Research article

Stochastic Extended Simulation (EXSIM) of M_w 7.0 Kumamoto-Shi earthquake on 15 April 2016 in the Southwest of Japan using the SCEC Broadband Platform (BBP)

M.C. Raghucharan[1],* and Surendra Nadh Somala[2]

[1] Department of Civil Engineering, Indian Institute of Technology, Hyderabad, Kandi, Sangareddy-502285, Telangana, India
[2] Department of Civil Engineering, Indian Institute of Technology, Hyderabad, Telangana, India

* Correspondence: Email: ce15resch11009@iith.ac.in; Tel: +919493105592.

Abstract: Ground motions for M_w 7.0, 15 April 2016, Kumamoto-Shi earthquake of Japan are simulated employing Stochastic Extended Simulation (EXSIM) methodology within the Southern California Earthquake Centre (SCEC) Broadband Platform (BBP) version 15.3.0, utilizing the strong ground motion data from K-NET and KiK-net. Residuals [(ln(data/model)] are plotted as a function of hypocentral distance for a subset of eight periods. Trail simulations are run by varying stress drop until a better match of residuals is obtained. Validation exercise is run with a new data set to ascertain the accuracy of simulations. The results exhibit a close match between the recorded and predicted data. Adopting the validated seismological model of this study, ground motions are predicted at three important sites, which are devoid of strong-motion stations. These results can be used as inputs for conducting dynamic, response spectrum analysis of structures, liquefaction potential of soils, stability analysis and landslide runout estimation of slopes.

Keywords: Kumamoto-Shi earthquake; ground motion simulation; SCEC BBP; EXSIM; Goodness-of-Fit plots

Abbreviations: SCEC: Southern California Earthquake Centre; GoF: Goodness-of-Fit; BBP: Broadband Platform; GMPE: Ground Motion Prediction Equations; RS: Response Spectra; GP: Graves & Pitarka; SDSU: San Diego State University; UCSB: University of California, Santa Barbara;

EXSIM: Stochastic Extended Simulation; CSM: Composite Source Model; SMSIM: Stochastic point source simulation; FINSIM: Finite fault simulation; K-NET: Kyoshin network; KiK-net: Kiban Kyoshin network; PSA: Pseudo Spectral Acceleration; NGA: Next Generation Attenuation; J-SHIS: Japan Seismic Hazard Information Station

1. Introduction

Japan is one of the world's highly seismically active regions on the planet due to its complex crustal structure where four tectonic plates meet around the boundary of Japanese Islands. About 1/10th of the earthquakes on the globe occur nearby Islands of Japan, which are due to collision and subduction of these four plates. Earthquakes in the Eastern part of Japan occur due to subduction of Pacific plate under the North American and Eurasian plate, and South-western part activity is due to the Philippine Sea plate descending beneath the Eurasian [1]. The region is characterized by the several huge earthquakes including the great Tohoku M 9.0 in 2011. The continuous interaction of these four plates makes the region highly seismic and volcano prone [2]. Seismic and volcanic hyperactivities of the region around Japan are characterized by structural divergence in the crust and upper mantle [3,4]. Hence, shallow earthquakes are predominant in Japanese Islands.

On 15 April 2016, an earthquake of magnitude M_w 7.0 occurred north of Kumamoto, in southwest Japan in the midst of foreshocks (M 6.2 and 6.0) and aftershocks in the same region. The peak ground acceleration of 1157 gals (cm/s^2) was measured at Mashiki town during this earthquake. Numerous structures collapsed and caught fire and few were severely damaged in the region of Mashiki which is 10 km away from Kumamoto city due to high ground acceleration and shallow depth of epicenter [5]. The earthquake was due to subduction of Philippine Sea plate beneath Japan and Eurasia plate at a velocity of 58 mm/yr, which killed 9 people and injured about 800. The earthquake was a result of strike-slip faulting at shallow depth. Fault mapping of the region revealed an east-west or northeast-southwest trend, which complies with right-lateral strike-slip faulting. The Philippine fault, which is over a length of 1200 km is seismically active and involved in major earthquakes of historic importance including M 7.6 Luzon earthquake of 1990 [6].

The boundary of the Philippine Sea plate which is considered as seismically more active has produced 7 Great (M > 8.0) earthquakes and 250 large (M > 7.0) events. The most catastrophic events in the list are 1923 Kanto, the 1948 Fukui and the 1995 Kobe (Japan) earthquakes with 99000, 5100 and 64000 causalities respectively, the 1935, the 1999 Chi-Chi (Taiwan), the 1976 M 7.6 Moro Gulf and 1990 M 7.6 Luzon (Philippines) earthquake are among the other [7]. Figure 1 shows the map of Japan region demarcated with plate boundaries and its major earthquake locations. As the seismic activity in this region is intense, a proper understanding of the response of structures is a paramount problem. Hence, modelling studies have been taken for this earthquake.

Simulation of strong motion data precisely in the broad frequency range (0.1 to 20 Hz) is vital in predicting PGA levels and generating synthetic accelerograms at locations other than recording stations. Fortunately, state-of-art broadband accelerographs are installed at the seismic sensitive regions of the world which use sophisticated technology for recording strong motion data accurately. Broadband ground motion simulations can generate synthetic accelerograms which can be utilised for dynamic analysis of structures, in the absence of real accelerograms. They also fill in the gap where there are fewer recordings for major magnitudes in the near field [9]. The primary objective of the paper is to simulate ground motions of 15 April 2016 M_w 7.0 Kumamoto-Shi earthquake, making use

of the SCEC BBP and validate them. Further, utilizing the validated seismological model of this study, acceleration time series and 5% damped Pseudo acceleration spectra (PSA) are generated in the frequency range of engineering interest, for sites where considerable damages occurred that lacked strong-motion stations, in Kyushu region of Japan.
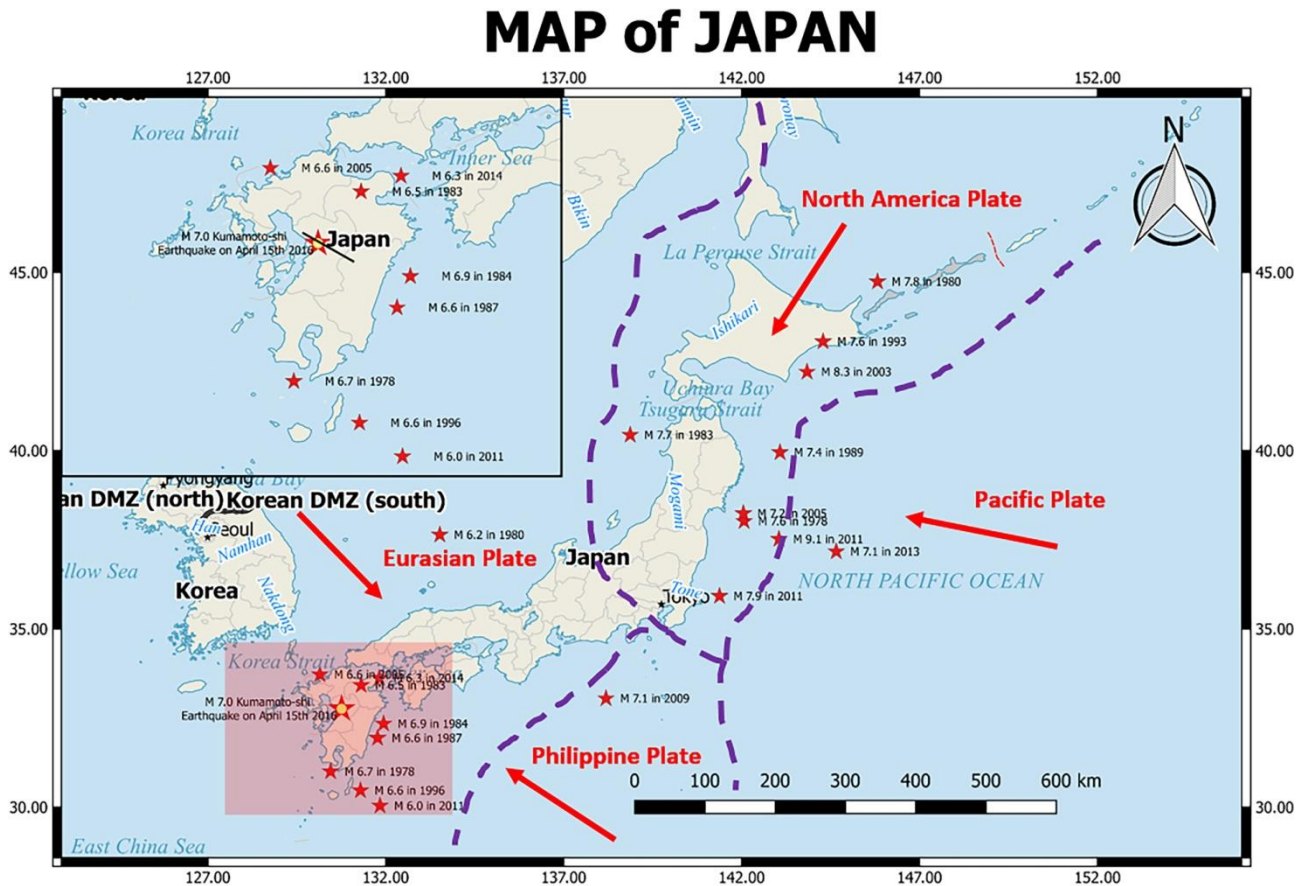
Figure 1. Map of Japan region showing major earthquake locations in red stars along with magnitude and year of occurrence. The small window at the left top corner shows the region of South-west Japan with the location of 15 April 2016 M_w 7.0 Kumamoto-Shi earthquake indicated by a big star with a yellow circle inside. The violet discontinuous lines indicate the plate boundaries of the four major tectonic plates meeting near Japanese islands [8]. The red arrows indicate the tentative direction of movement of respective plates. The solid black line shows the trace of the fault that caused the earthquake.

A building, a bridge and a tunnel site that are devoid of strong-motion stations, are selected to assess the ground motions, that were damaged during the earthquake. A popular tourist destination in Kumamoto, the Kumamoto castle suffered severe damages to the stone walls and roof. Significant damages also occurred to the Great Aso Bridge due to the event and landslide post-earthquake. Shear cracks developed in the Tawarayama tunnel and several concrete lining elements fell causing a massive threat to the stability of tunnel [10].

The present work was run on an Intel i7 processor with 4GB RAM, which took 15 minutes for each simulation. With the advent of high performance computing facilities, enough simulations can be

run for developing GMPE. In the past, seismological models which simulate acceleration time histories were used for deriving GMPEs, in the absence of strong motion data [11–15].

2. Simulation methods

Different methods have been proposed by pioneers in this field for simulating ground motions. The first class of methods to simulate the accelerograms is by filtering and windowing Gaussian noise which is based on random-vibration theory [16,17]. A different approach in the same path is to match the simulated response spectra with the target response spectrum [18–20].

Another class of methods for strong ground motion simulation involves a physical approach employing source, path, and site effects. Source intricacy was addressed by empirical Green's functions [21,22] and stochastic sub-event summation approach [23–26]. A more advanced, if not accurate, class of methods are numerical solutions to 3D Wave propagation equation which is based on finite-difference method [27] used by Graves [28], Pitarka [29], Aoi and Fujiwara [30], Moczo et al. [31], Lee et al. [32], or spectral element methods [33] employed by Komatitsch et al. [34], Priolo [35], Komatitsch et al. [36], Lee et al. [37] and Stupazzini et al. [38] for ground motion simulation.

Software tools with high computing capabilities are the best option for simulating ground motions accurately. Various ground motion simulation programs were developed by researchers to meet the requirement by employing finite-fault approach, and hybrid deterministic-stochastic methods. These programs use a different set of input files which is a principal drawback leading to an unfair comparison between them. A group of researchers teamed together to develop a single program which serves the purpose and eligible for fair comparison. One of the outcomes of these efforts was the BBP developed by the Southern California Earthquake Centre (SCEC).

Southern California Earthquake Centre developed an open-source program, known as the SCEC BBP for simulating strong motion data from earthquakes. The platform was first introduced in the year 2013 and underwent many software updates over these years such as updating 4 simulation methods (GP, SDSU, UCSB, and CSM), integrating multiple post-processing codes, adding 4 GMPEs of NGA-West 2 and 3 GMPEs of NGA-East [39]. The main advantage of the BBP lies in its varied applicability for different regions like US, Canada, and Japan where earthquakes are more frequent. Presently, version 15.3 is the latest and was used for simulating the strong motion data of 15 April 2016 M_w 7.0 Kumamoto-shi, Japan earthquake.

Several scientific methods were included in the platform namely, Graves & Pitarka (GP) [40], San Diego State University (SDSU) [41], University of California, Santa Barbara (UCSB) [42], Stochastic Extended Simulation (EXSIM) [43] and Composite Source Model (CSM)—under development [44] which the user can select for generating the synthetics. Comparisons with the recorded data are performed using two Goodness-of-Fit (GoF) modules. Available GoF modules on the platform are GP and SDSU. GoF comparisons are performed mainly by comparing the response spectra of calculated seismograms with the observed seismograms. The stations which do not have observed seismograms data will not be included in the automatically generated GoF comparisons.

2.1. Methodology

The present study employs EXSIM methodology of the platform. EXSIM is an extended stochastic finite-fault simulation methodology proposed by Motazedian and Atkinson [43], which is a

developed form of SMSIM (Stochastic point source simulation) proposed by Boore [45,46] and FINSIM (Finite fault simulation) proposed by Beresnev and Atkinson [25,47]. In the past, the same methodology was successfully used in simulating ground motions for 1980 Irpinia earthquake [48], 2003 Bam earthquake [49], 2008 Iwate-Miyagi Nairiku earthquake [50], 2011 Tohoku, Japan earthquake [51] and 2015 Nepal (Gorkha) earthquake [52].

Stochastic point source model assumes the source process is concentrated at a single point and the acceleration time series generated at a site carry both deterministic and stochastic faces of ground motion. The deterministic part which is a function of both magnitude and distance is specified by Fourier spectrum and the stochastic aspects are obtained by treating the motion as noise. This methodology worked well only when the hypocentral distance is much larger than the source dimension. The total point source spectrum is calculated by the Eq 1 [53]:

$$Acc\ (Mo, R, f) = Source\ (Mo, f)\ Path\ (R, f)\ Site\ (f) \tag{1}$$

Where Acc (Mo, R, f) represents the total point-source spectrum observed at site; Source (Mo, f) represents the source spectrum at unit distance; Path (R, f) is the path effects which includes both geometric spreading and inelastic attenuation; Site (f) represents the site effects; M_o is the seismic moment [54]; R is the hypocentral distance and f is the frequency.

The key factor that determines the ground motions which are not included in the stochastic point source model is the effect of faulting geometry, distributed rupture, and rupture heterogeneity. To include these in the modelling of ground motions, Hartzell [21] proposed subdividing the fault into several small grids, which are treated as point sources. These sub-source contributions are summed up at the observation site, with proper delays. This methodology was coded into FINSIM by Beresnev and Atkinson [25,47]. Later, Motazedian and Atkinson [43] introduced the concept of dynamic corner frequency to reduce the dependencies to sub source size. This, in turn, eliminated multiple triggering of sub-events. The sub source dependency was terminated by Boore [55] with modification to sub-event normalization. This methodology was named as EXSIM and implemented in the BBP by Southern California Earthquake Centre [56]. The major advantage of EXSIM over FINSIM is its insensitivity to sub-fault size, conservation of energy radiated during the rupture process and only a portion of fault will be active at any given point of time [57].

The algorithm of EXSIM is:

$$Acc_{tot}(t) = \sum_{i=1}^{N} H_i \ x \ Acc\ (t - \Delta t_i - T_i) \tag{2}$$

Where Acc_{tot} (t) is the total seismic signal; H_i is the normalization factor for the ith sub source; Acc (t) is the signal of ith sub source; N is the total number of sub-sources; Δt_i is the time delay of sub source; T_i is a fraction of rise time.

$$H_i = \left(N \sum \left\{ f / \left[1 + \left(\frac{f}{f_0} \right)^2 \right] \right\}^2 / \sum \left\{ f / \left[1 + \left(\frac{f}{f_{0i}} \right)^2 \right] \right\}^2 \right)^{1/2} \tag{3}$$

Where f_0 is corner frequency; f_{0i} is the corner frequency of the ith sub source; and f is counter over frequency.

2.2. Strong motion data

Strong motion data has been acquired from K-NET and KiK-net which is Japan's nation-wide strong-motion seismograph network consisting of more than 1,000 observation stations distributed uniformly every 20 km. Instrumentation used for both the networks are same. The sensor type used is V403 or V404 tri-axial force-balance accelerometer with a natural frequency of 450 Hz and damping factor of 0.707. The sampling rate for stations recorded by K-NET and KiK-net are 100 and 200 samples per second respectively [58].

2.3. Source parameters

To carry out simulations for an earthquake, the main set of inputs are, the source file containing the moment magnitude, hypocentral location in latitude and longitude, and fault geometry, the station file containing longitude, latitude, station code and shear wave velocity V_{S30} for all the stations. V_{S30} is the average shear wave velocity in the top 30 m of the subsurface profile. Apart from these, the platform also need the 3-component acceleration time histories of real accelerograms for generating comparison plots between recorded and synthetic data.

The seismic moment, strike, dip, and rake are fixed to be 4.46×10^{26} dyne-cm, 128°, 74° and -14° based on global CMT. The fault dimensions, the location of hypocentre and depth to the top of fault for the Kumamoto-Shi, Japan earthquake are fixed to be 42 km in length and 18 km wide, -12 km and 11 km along strike and dip, and 2 km respectively based on Asano and Iwata [59]. The fault of size 42×18 km is discretised into 2×2 km size sub-faults (189 in total), and the slip weights are obtained from Asano and Iwata [59] for this earthquake. The stress drop is fixed based on different trial simulations made between values from 75 to 125 bars until a better match for residuals were obtained. The stress drop of 114 bars gave best results which was used for validation with a new set of data [60]. The sub source window is selected as Saragoni-Hart taper window for time-modulating Gaussian white noise. The epsilon and eta values of the tapered window are fixed as 0.35 and 0.15 respectively. The velocity with which the rupture propagated during this event, rupture velocity (V_{rup}) is obtained from literature as 2.4 km/s [59]. The sub surface structure of entire Japan had been digitalized and available on J-SHIS (Japan Seismic Hazard Information Station) website [61]. The shear wave velocity (V_s), density is obtained from the website for southwest Japan region as 3.41 km/s and 2.75 g/cm^3 respectively and the ratio of V_{rup}/V_s ~0.7. The rise time is taken as the inverse of sub source corner frequency ($1/f_0$). The pulsing percentage is the maximum percentage of the fault that may be active at any time which describes how much the fault plane is slipping at any moment in time. It is assigned a large aleatory variability from 10% to 90%. This parameter does not exert a significant influence on simulated amplitudes at most frequencies [57]. A median value of 50% has been assumed while running simulations.

The total path duration is calculated based on Edwards and Rietbrock [62] as

$$t = \begin{cases} 9.52 + 0.8 * R, & R \leq 50 \ km \\ 49.52 + 0.02 * (R - 50), & R > 50 \ km \end{cases}.$$

2.4. Path parameters

The geometric spreading parameter for southwest Japan region is taken from literature Edwards

and Rietbrock [62] as $G = \begin{cases} \dfrac{1}{R}, & R \le 30\ km \\ \dfrac{1}{R^{1.27}}, & 30 \le R \le 110\ km \\ \dfrac{1}{R^{1.59}}, & R > 110\ km \end{cases}$ and quality factor for the region of

study is taken from Petukhin et al. [63] as Q = 180 f$^{0.7}$.

2.5. Site parameters

H/V ratio method even though does not capture the entire site amplification but only predominant frequency, it fairly predicts the amplification of a site, especially for the sites in the proximity of the epicenter. In the absence of a reference rock-site stations or bore hole arrays, the H/V ratio serves as a practical alternative to the standard site amplification estimation A(f) [64–67]. The overall site effects term, site (f) is obtained by multiplying A(f) with near-surface attenuation term, D(f) = $e^{-\pi K_v f}$. Where K_v is Kappa factor, which characterizes near-surface attenuation [68].

The crustal amplification factors were worked out with the regional velocity model for Kumamoto region from J-SHIS website [61] using quarter wavelength technique, and the variation of crustal amplification factor with frequency is shown in Figure 2.
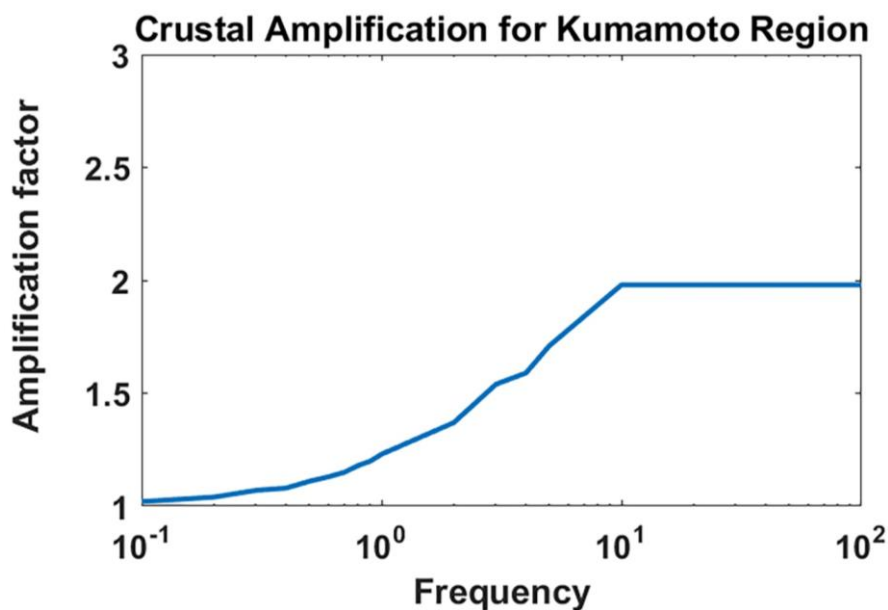
Figure 2. Variation of crustal amplification factor with frequency for Kumamoto region.

Kappa value is fixed as 0.035 based on Chen and Atkinson [69]. The response spectra are computed at 5% damping. Time step is fixed as 0.01 as per the observational data. Finally, V_{S30} values were obtained from site data application (1.3.2) developed by the University of Southern California and OpenSHA.org based on the topographic slope [70]. The input parameters included for running the simulation are given in Table 1.

The details of the station name, latitude, longitude, epicentral distance and V_{S30} values are given in Table 2.

**Table 1.** Source, path and site parameters of the 15 April 2016 Kumamoto-Shi Japan earthquake simulation.

Source	
Magnitude (M_w)	7.0
Fault geometry	42×18 Km
Slip model	Slip weights from Asano and Iwata (2016)
Slip model seed	platform-specified
Subsource size	2×2 Km
Stress Drop	75–125 bars
Subsource window	Saragoni-Hart ($\varepsilon = 0.35$, $\eta = 0.15$)
Vrup/Vs	0.7
Rise time	$1/f_o$
Pulsing %	50%
Subsource duration, t	$= 9.52 + 0.8 \times R$ R up to 50 km
	$= 49.52 + 0.02 (R{-}50)$ R > 50 km
Path	
Geometric spreading	R^{-1} up to 30 km and $R^{-1.27}$ between 30 and 100 km and $R^{-1.59}$ beyond 110 km
Anelastic attenuation	$Q(f) = \max (150, 180\ f^{0.7})$
Shear wave velocity	3.41 km/s
Density	2.75 g/cc
Site	
Site amplification crustal amplification	Average of H/V ratios for all stations
Kappa	0.035 (high-frequency fall off slope)

Table 2. Station metadata for the simulated stations of 15 April 2016 Kumamoto-Shi Japan earthquake.

Sl.No.	Name of the Station	Station Code	Longitude	Latitude	Epicentral distance (km)	Vs 30 (m/s)
1	CHIKUSHINO	FKO009	130.5163	33.4952	85.67	370.5520
2	AMAGI	FKO010	130.6689	33.4235	75.08	420.5705
3	UKIHA	FKO012	130.7939	33.3319	64.46	444.0663
4	YAME	FKO013	130.5607	33.2252	55.78	258.9047
5	IZUMI	KGS002	130.3519	32.0916	83.03	285.5654
6	YAMAGA	KMM002	130.6846	33.0185	30.40	333.2913
7	HITOYOSHI	KMM016	130.7757	32.1966	61.90	365.9602
8	TARAGI	KMM017	130.9257	32.2561	57.36	283.7520
9	SHINWA	KMM020	130.1807	32.3636	69.61	420.0199
10	AMAKUSA	KMM021	129.9997	32.3793	82.67	389.8910
11	TAKACHIHO	MYZ001	131.3089	32.7050	51.45	394.2328
12	NANGOH	MYZ004	131.3339	32.3889	67.19	520.2060
13	EBINO	MYZ009	130.8110	32.0461	78.76	197.8679
14	KOBAYASHI	MYZ010	130.9721	31.9968	86.40	317.7205
15	SHIIBA	MYZ020	131.1470	32.4550	48.99	613.0866
16	KUCHINOTSU	NGS014	130.1849	32.6106	56.30	323.1902
17	AMAGASE	OIT008	131.0203	33.2555	60.87	447.1545
18	KARATSU	SAG002	129.9195	33.4247	108.38	468.9557
19	FUJI	SAG003	130.2074	33.3730	86.19	524.8462
20	KASHIMA	SAG008	130.0996	33.1038	73.12	340.2311

Observational data from 20 stations were used in running simulations. A map view of the simulation region showing the locations of recording stations used in the simulation along with fault plane and epicenter are shown in Figure 3.
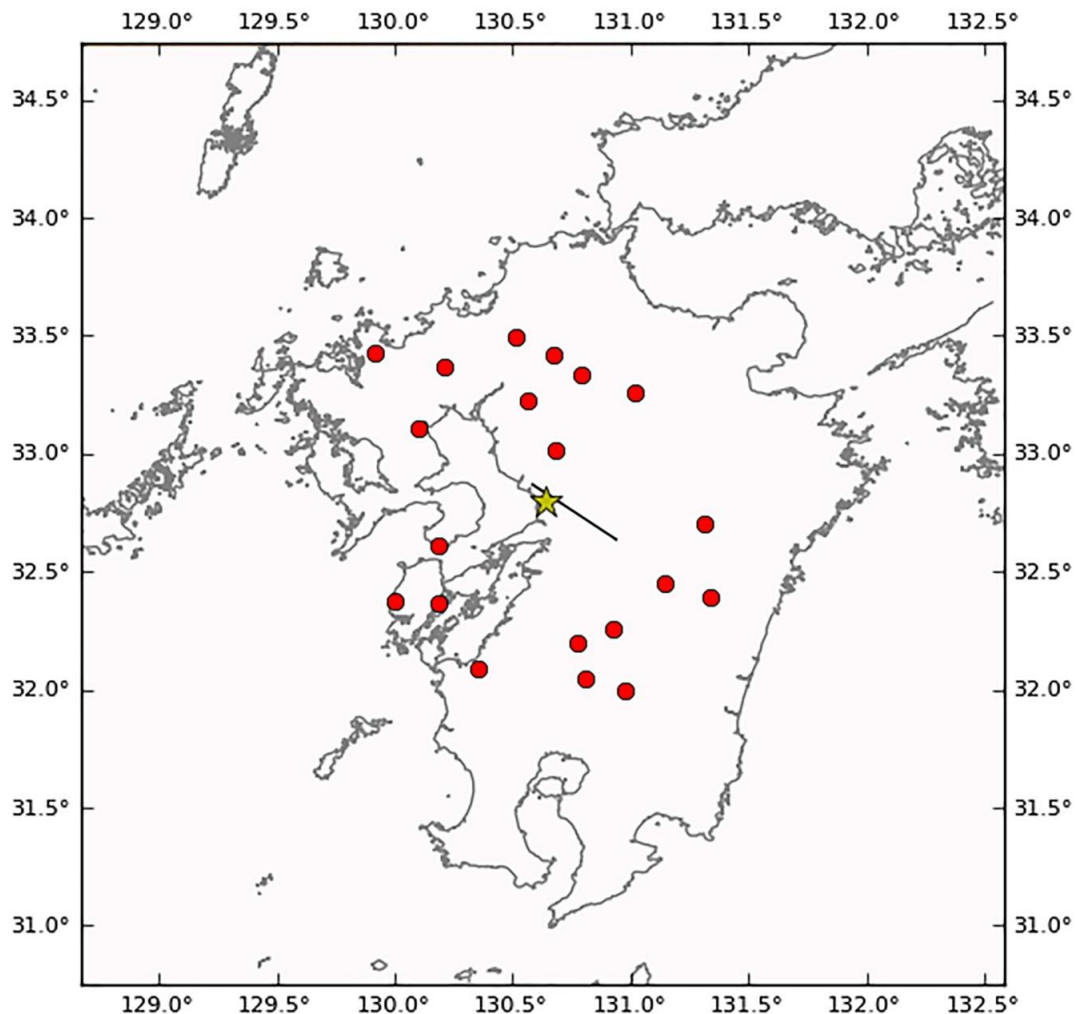

Figure 3. Map generated in broadband platform showing the fault trace and hypocentre (indicated by a star) along with the locations of recording stations in red colour.

3. Results and discussions

Simulations for 15 April 2016 Kumamoto-Shi Japan earthquake, were run with EXSIM method. Figures 4 and 5 shows the simulated acceleration and velocity time histories respectively along N-S, E-W, and U-D, at sample station Taragi, generated by the platform.

A combined plot showing the actual data and the synthetic velocity time series along with the Husid plot (normalized Arias intensity as a function of time) along the two horizontal directions are generated for each station to make sure the waveforms look reasonably well. The plot for a sample station, Taragi is shown in Figure 6. The plot in Black colour corresponds to actual data, and in red corresponds to synthetic data. The normalized Arias intensity plot shows a good resemblance of synthetics produced by the BBP with the actual data.
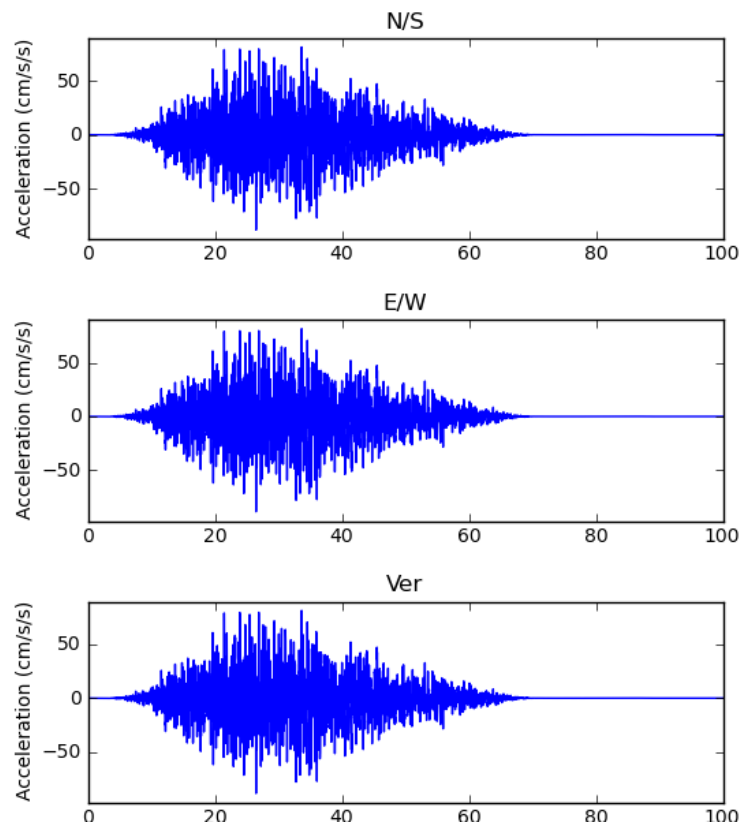
Figure 4. Synthetic acceleration time histories for TARAGI (KMM017) station generated by the platform.
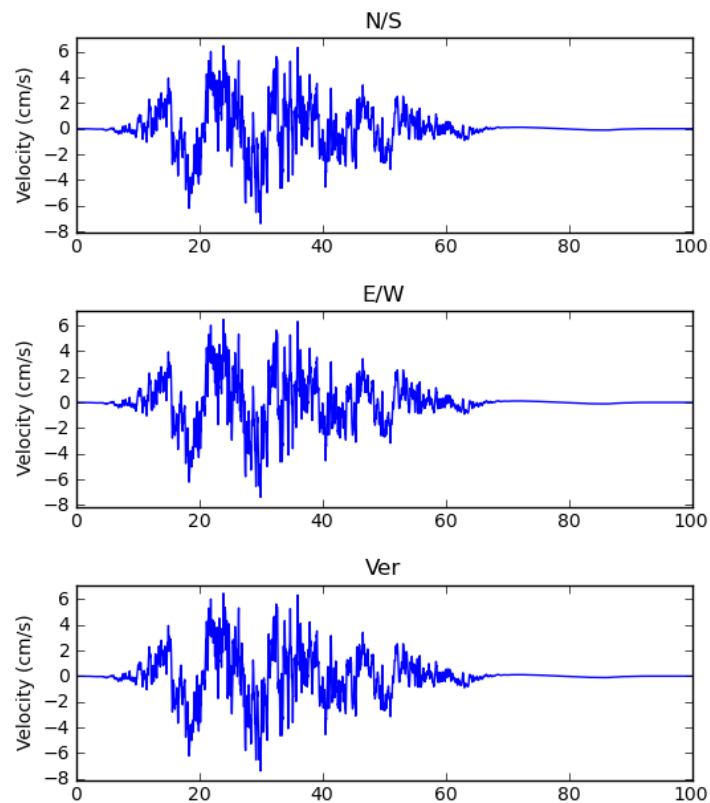

**Figure 5.** Synthetic velocity time histories for TARAGI (KMM017) station generated by the platform.
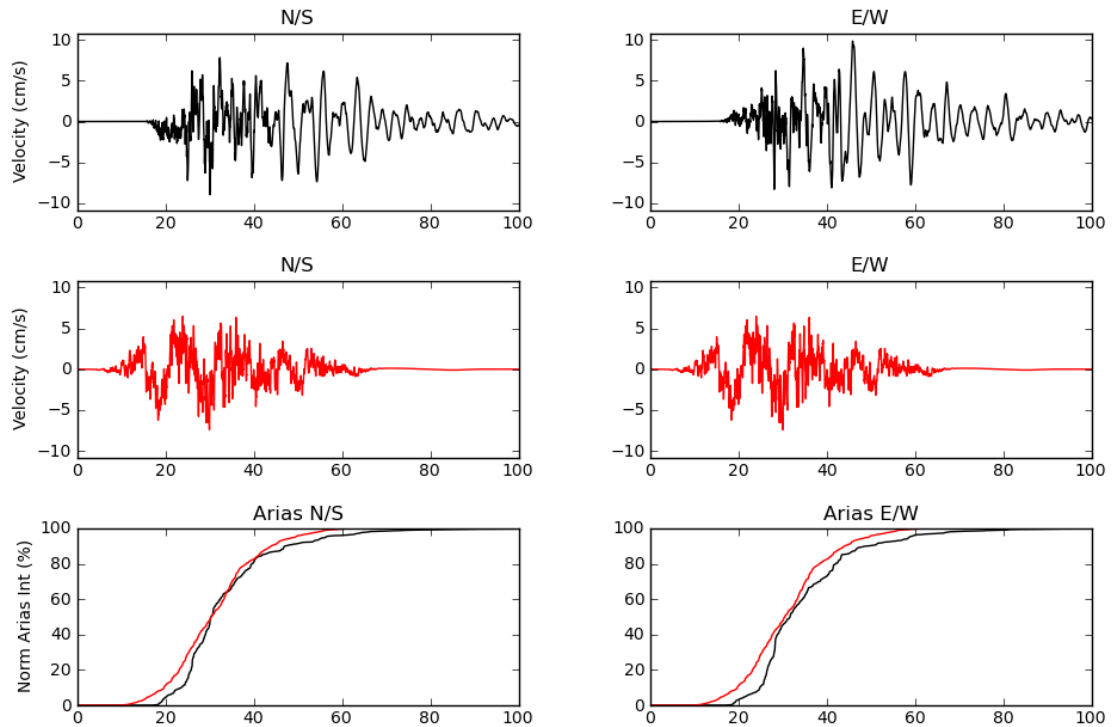
Figure 6. Plot showing the temporal evolution of actual velocity, simulated velocity and Normalized Arias intensity (%) for N-S and E-W components for TARAGI (KMM017) station. The plot in Black colour corresponds to actual data and in red corresponds to synthetic data.

The BBP calculates response spectra for the two horizontal components, and RotD50 [71] (which is an average median horizontal component Pseudo Spectral Acceleration (PSA)) for periods ranging from 0.01 to 20 seconds. Figure 7 shows the comparison of PSA spectra (5% damping) for the simulated time-series against that of the recordings of Kumamoto-Shi earthquake, calculated by RotD50 module for N-S, E-W directions, and the RotD50 component for the Taragi station. The blue line indicates actual data and green line for synthetic data. The response spectra of simulated time histories are in good compliance with those of actual data.
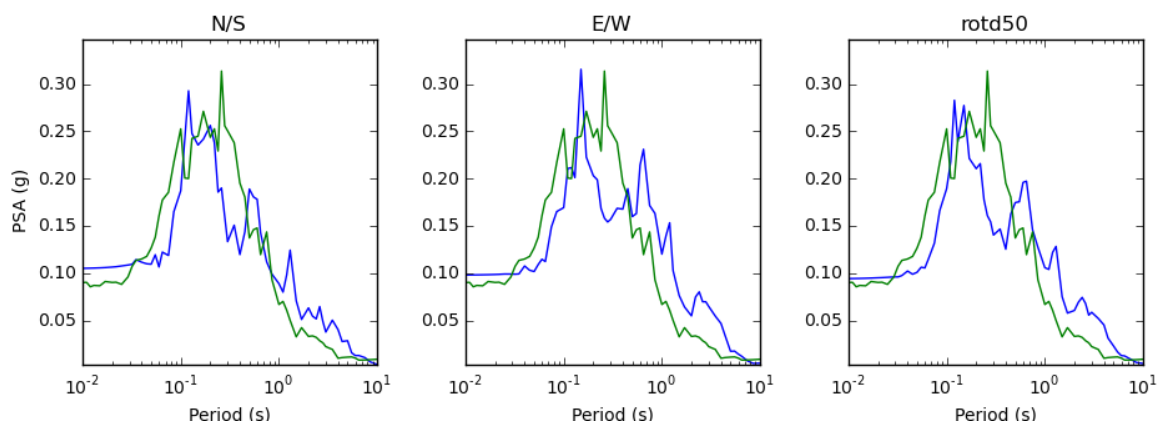

Figure 7. Plot showing the response spectra for TARAGI (KMM017) station calculated by RotD50 module for all the three components.

Along with this, the platform also generates several GoF comparisons. The prime comparison is a residual plot also known as distance-based GoF plot. The residual here is defined as the natural logarithm of the ratio of PSA of observed to PSA of synthetic data computed by RotD50 module for a given period. Residuals are computed for 112 time periods (between 20 to 0.01 sec.) and are plotted as a function of hypocentral distance for a subset of eight (0.01, 0.05, 0.1, 0.2, 0.5, 1.0, 2.0 and 5.0 seconds) time periods (Figure 8). The residuals shown in Figure 8 for different periods are distributed around zero. Positive residuals indicate under prediction by the model, and negative residuals indicate over prediction.
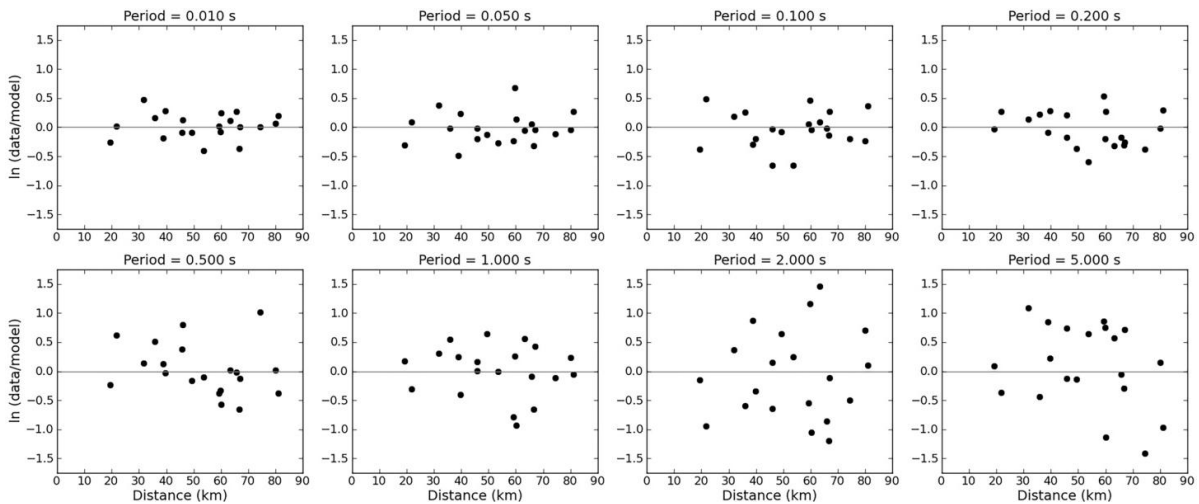

Figure 8. Goodness-of-Fit of 15 April Kumamoto-Shi earthquake simulations for eight periods between response spectra of observed data to model as a function of hypocentral distance using RotD50 module for twenty stations. The black dots above zero line indicate under prediction and below zero indicate over prediction by the platform.
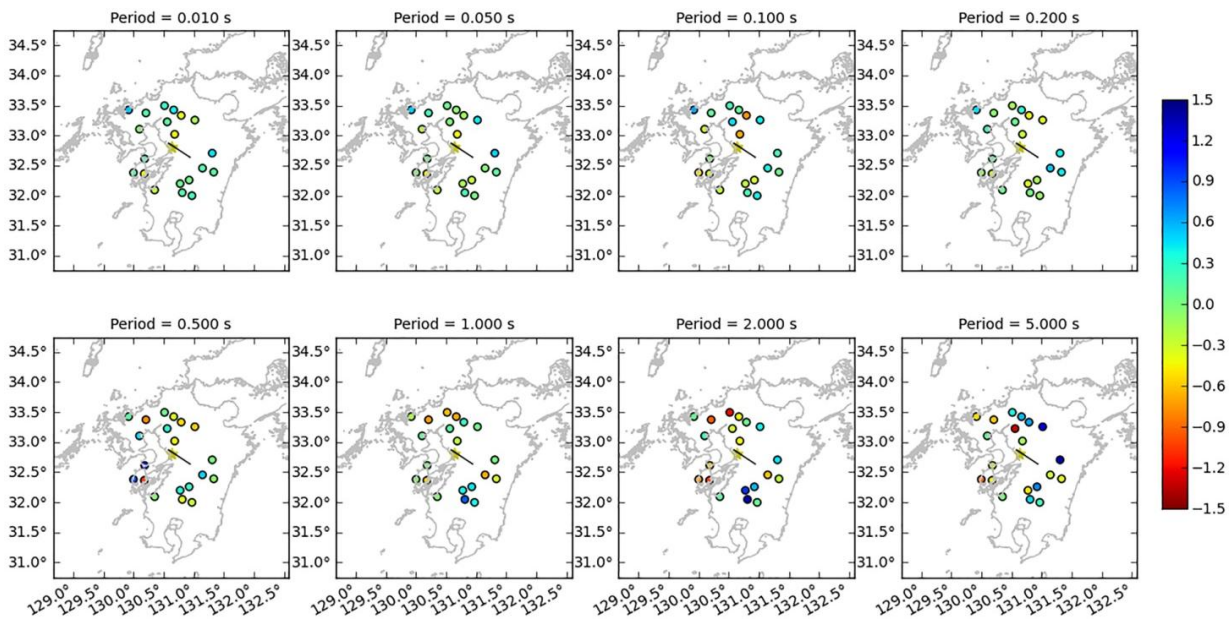
Figure 9. Plot showing Goodness-of-Fit on a colour coded map with GoF values computed at station locations for selected periods.

Residuals are also plotted for the same subset of time periods as a map view to identify their spatial distribution (Figure 9). Neither the residuals in Figure 8 nor those in Figure 9 seem to display any pattern.

The average GoF metric computed for all stations using the RotD50 module as a function of the time period (from 0.01 to 10 seconds) is shown in Figure 10. The red line corresponds to the mean GoF over all stations of this earthquake. The narrow band in yellow, which is 90% confidence limit, indicates the mean is well constrained by data. The close proximity of the solid red curve in this plot suggests the simulations are effectively predicting the data.
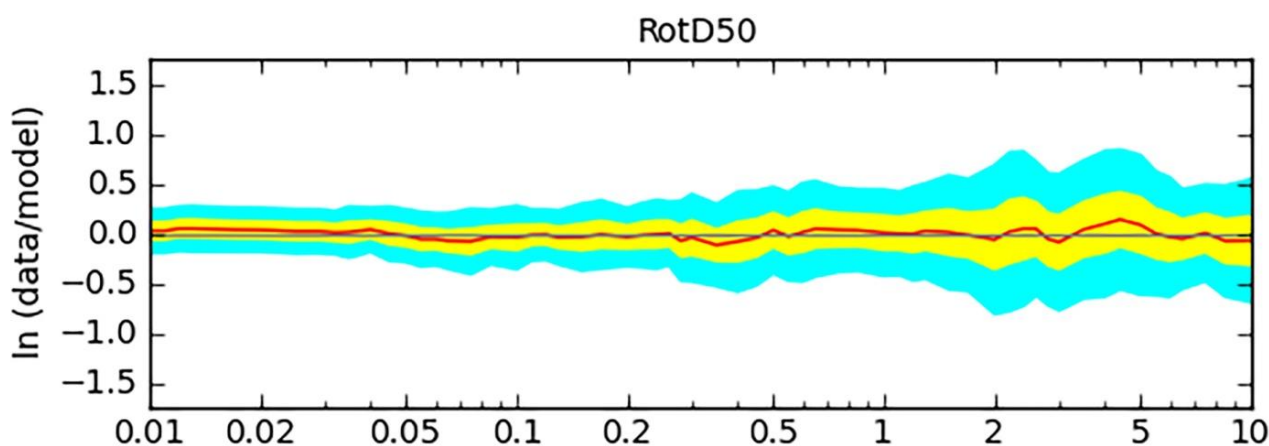
Figure 10. Plot showing Goodness-of-Fit averaged over all the stations as a function of time period using RotD50 module. The solid line is the mean, the narrow band in yellow colour is 90% confidence interval of mean, and the wide band in cyan colour shows the standard deviation centered around the mean.

Figure 11 shows the comparison plots of the simulated data against the GMPE models existing in the BBP. The platform has 3 GMPE sets, NGA-West 1, NGA-West 2 and CENA Group 1. Out of the three GMPE sets, NGA-West 2 is predicting close to data which was shown below. 4 built-in GMPE models for NGA-West 2 was developed by Abrahamson et al. 2014 [72] (ASK14), Boore et al. 2014 [73] (BSSA14), Campbell and Bozorgnia 2014 [74] (CB14) and Chiou and Youngs 2014 [75] (CY14). Out of the four GMPE plots, the GMPE developed by Boore et al. 2014, (BSSA, 2014) is in good agreement with the synthetic data generated during simulations.
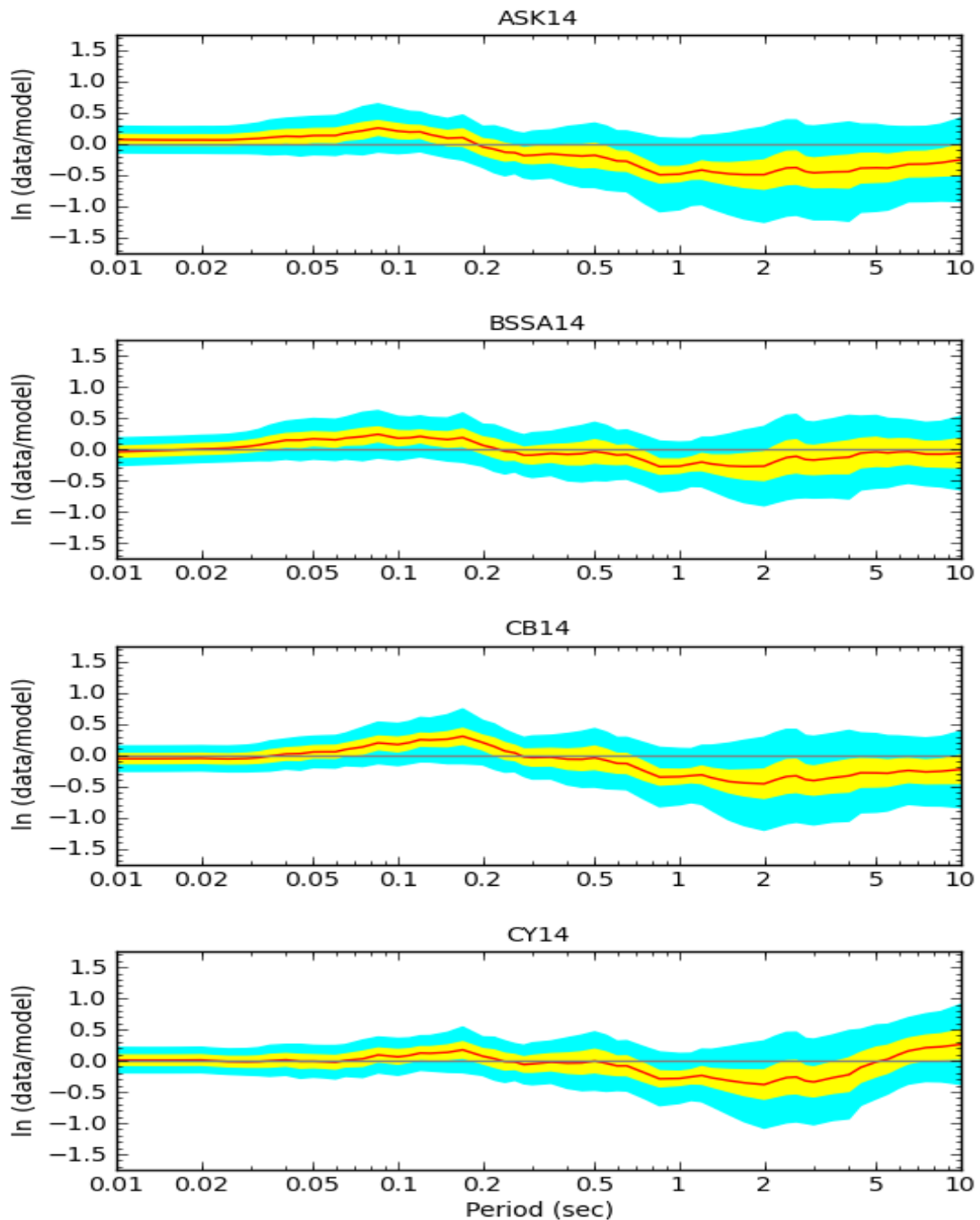
Figure 11. Comparison of the Validation data of 15 April Kumamoto-Shi earthquake against different Ground Motion Prediction Equation (GMPE) models proposed by Abrahamson et al. (ASK14), Boore et al. (BSSA14), Campbell-Bozorgnia (CB14) and Chiou-Youngs (CY14).

To validate the results, a new set of data from 12 stations were utilised and ran in BBP. The metadata of 12 stations along with the obtained PGA values from validation is given in Table 3 and plotted in Figure 12. The PGA residuals in the plot are close to zero line which indicates very good compliance between recorded and predicted values.

Table 3. Metadata of stations used for validation along with predicted values of PGA and computed residuals.

Sl.No	Station Name	Station Code	Longitude	Latitude	Epi-central distance (km)	Vs 30 m/s	Recorded PGA cm/s^2	Predicted PGA cm/s^2	Residuals ln(Recorded/Predicted)
1	KITAKYUSHU	FKOH01	130.9798	33.8849	127.5	395.1	15.5	16.8	−0.08
2	MIYANOJO	KGS005	130.4513	31.9006	99.2	367.0	65.4	43.5	0.41
3	OHZU	KMM005	130.8774	32.8761	17.4	445.3	482.3	409.8	0.16
4	UTO	KMM008	130.6582	32.6878	12.1	213.1	771.1	883.6	−0.14
5	YABE	KMM009	130.9856	32.6858	22.2	381.2	639.5	540.9	0.17
6	TOMOCHI	KMM011	130.8652	32.6167	18.0	386.8	602.4	642.1	−0.06
7	TANOURA	KMM013	130.5099	32.365	49.2	385.5	137.8	132.8	0.04
8	KAWAMINAMI	MYZH08	131.5309	32.2132	93.9	354.8	28.7	37.8	−0.28
9	KITSUKI	OIT007	131.6142	33.4169	108.4	322.0	42.5	26.4	0.48
10	TAKEDA	OIT015	131.397	32.9722	64.1	289.4	76.6	69.6	0.10
11	NOTSUHARA	OITH05	131.542	33.1525	85.3	760.0	31.6	42.5	−0.29
12	KOKONOE	OITH11	131.2118	33.2844	72.5	462.6	66.6	65.6	0.01

PGA Residual Plot of New Stations (Validation)
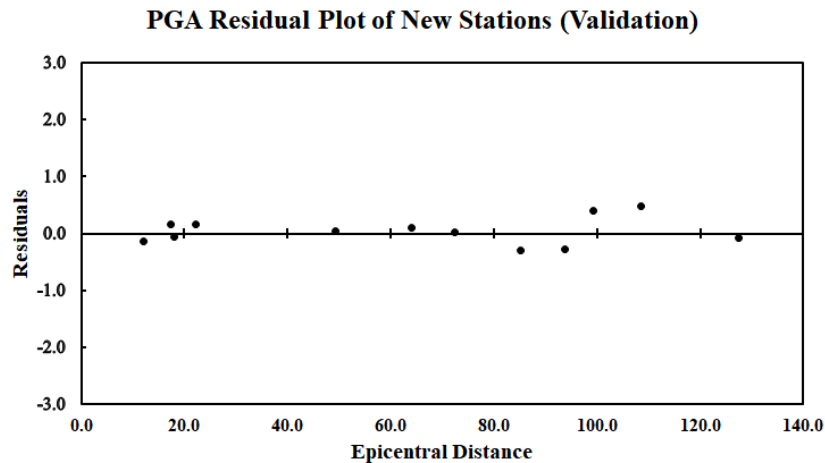
Figure 12. Plot of PGA residuals [ln(recorded/predicted)], for 12 stations used in validation exercise. The residuals are close to zero which indicate good compliance between recorded and predicted values.

Further, the residuals (Goodness-of-Fit Plot) of PSA at eight periods as a function of hypocentral distance for 12 stations is generated within BBP and shown in Figure 13. The residual at different periods shown in the plot are distributed around zero, which illustrate fair prediction of simulations conducted for Kumamoto earthquake within SCEC BBP.
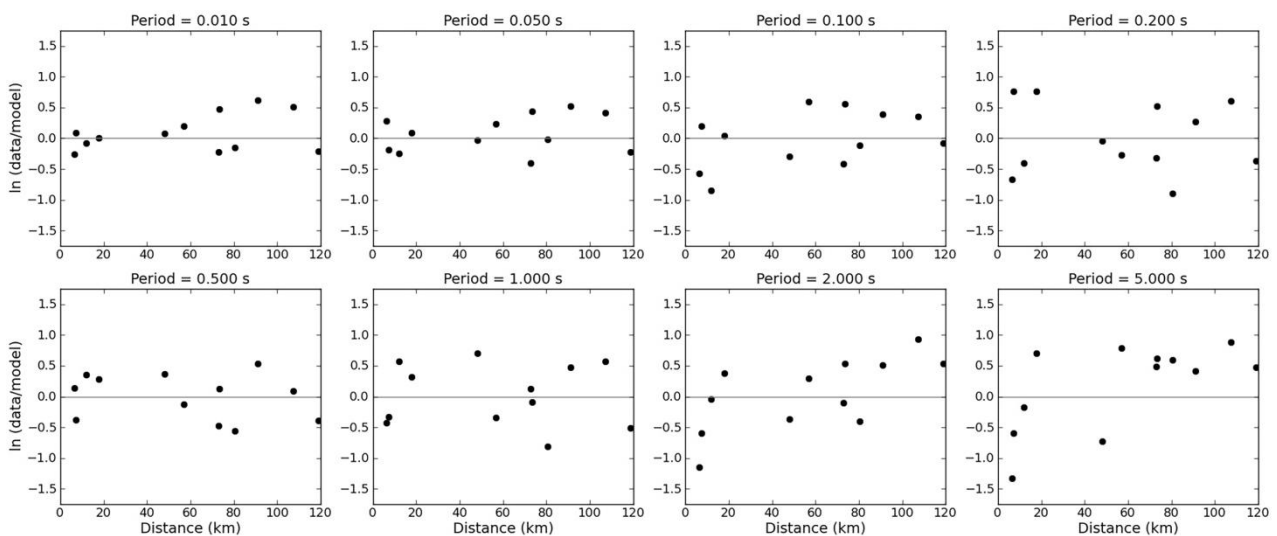
Figure 13. Goodness-of-Fit Plot of PSA residuals [ln(data/model)] for 12 stations used in validation exercise are reported at eight periods. The residuals (black dots) are distributed around zero which indicate a fair prediction of simulations.

Utilizing the validated seismological model of this study, we generated acceleration time series and 5% damped PSA in the frequency range of engineering interest, at three sites: The Kumamoto castle, the Great Aso bridge and the Tawarayama tunnel, where considerable damages occurred that lacked strong-motion stations, in Kyushu region of Japan. Figure 14 shows the acceleration time series and 5% damped PSA at the selected locations.
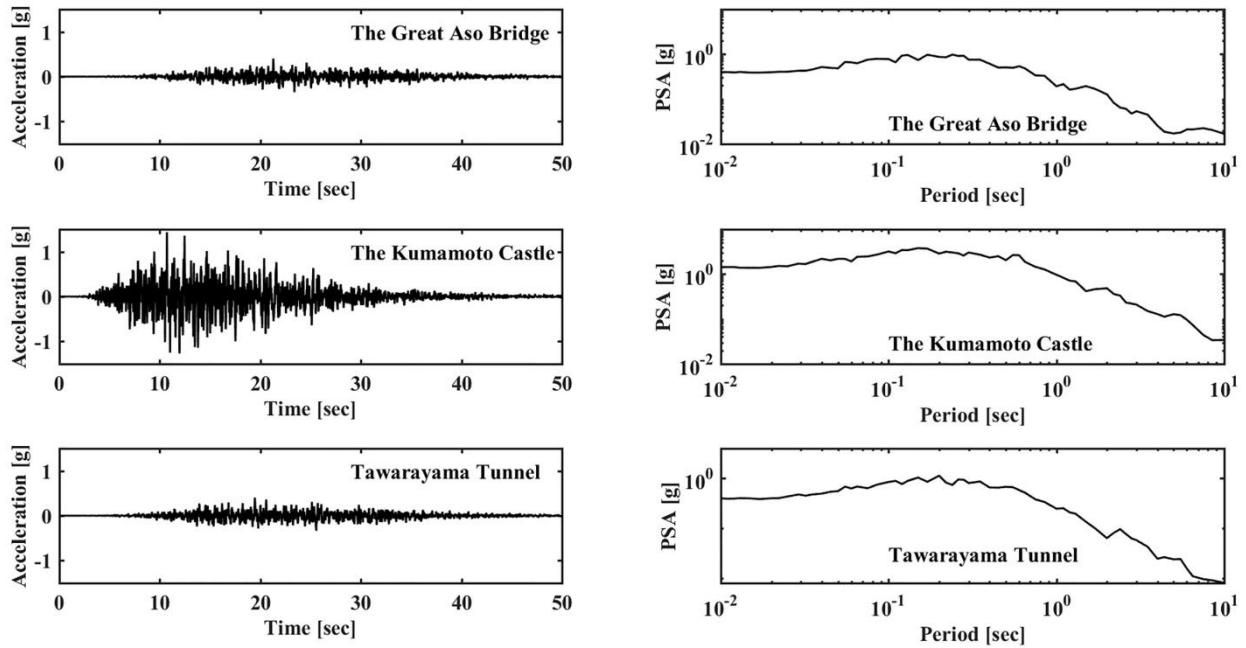
Figure 14. Acceleration time series and 5% damped PSA at three sites, the Great Aso bridge, the Kumamoto castle, and the Tawarayama tunnel respectively.

The PGA at the Kumamoto castle is more than 1 g due to its proximity to the earthquake source. Even though the PGA of the Great Aso bridge site is considerably less that Kumamoto castle site, the landslide post-earthquake might have contributed to its significant damage. Being an underground structure, the tunnel is susceptible to slope failures, ground subsidence, liquefaction and soil-structure interaction effects during an earthquake. Hence, this signifies the importance of multi-hazard assessment on infrastructure in Japan.

These results can be employed for conducting dynamic and response spectrum analysis of structures in the damaged regions, for earthquake resistant design. Further, these results can also be utilized as inputs for evaluating liquefaction potential of soils, analysis of slope failures and landslide runout estimation, as the earthquake triggered numerous landslides in the nearby mountainous areas of Kyushu region [76].

4. Conclusions

Simulation of ground motions was conducted for the M_w 7.0 Kumamoto main shock utilising recordings at 20 stations using SCEC BBP. Residuals at several time periods are shown to be unbiased. Additionally, the spatial variation of residuals at low to high time periods doesn't exhibit any pattern. Furthermore, the goodness-of-fit at all time-periods for the average horizontal is obtained close to zero. The BSSA 14 appears to have better agreement with the data, more so for shorter periods (periods less than 1 sec) where response spectrum usually exhibits peak values.

Validation exercise is run for a new set of data to check the accuracy of Kumamoto earthquake simulations. Finally, we generated ground motions for three severely damaged locations of Kyushu region in Japan, the Kumamoto castle, the Great Aso Bridge and the Tawarayama tunnel, with the validated seismological model. The ground motions obtained can be considered as input for dynamic,

response spectrum analysis of structures, liquefaction potential of soils, stability analysis and landslide runout estimation of slopes.

Acknowledgments

Conflicts of interest

All authors declare no conflicts of interest in this paper.

References

1. Zhao D, Ochi F, Hasegawa A, et al. (2000) Evidence for the location and cause of large crustal earthquakes in Japan. *J Geophys Res Solid Earth* 105: 13579–13594.
2. Sun A, Zhao D, Ikeda M, et al. (2008) Seismic imaging of southwest Japan using P and PmP data: Implications for arc magmatism and seismotectonics. *Gondwana Res* 14: 535–542.
3. Zhao D, Kanamori H, Negishi H, et al. (1996) Tomography of the source area of the 1995 Kobe earthquake: Evidence for fluids at the hypocenter? *Science* 274: 1891–1894.
4. Zhao D, Wang Z, Umino N, et al. (2007) Tomographic imaging outside a seismic network: Application to the northeast Japan arc. *Bull Seismol Soc Am* 97: 1121–1132.
5. EERI KUMAMOTO JAPAN EARTHQUAKE CLEARINGHOUSE: M7.0 APRIL 15, 2016 AT 16:25:06 UTC. Available from: http://www.eqclearinghouse.org/2016-04-15-kumamoto/2016/04/22/ground-motions-of-the-2016-kumamoto-earthquake/.
6. Yoshida Y, Abe K (1992) Source mechanism of the Luzon, Philippines earthquake of July 16, 1990. *Geophys Res Lett* 19: 545–548.
7. USGS Seismicity of the Earth 1900-2012, Philippine Sea plate and vicinity: Open-File Report 2010-1083-M. Available from: https://pubs.usgs.gov/of/2010/1083/m/.
8. Simutė S, Steptoe H, Cobden L, et al. (2016) Full-waveform inversion of the Japanese Islands region. *J Geophys Res Solid Earth* 121: 3722–3741.
9. Burks LS (2015) Ground motion simulations: *Validation and application for civil engineering problems* (Doctoral dissertation, Stanford University).
10. Bhattacharya S, Hyodo M, Nikitas G, et al. (2018) Geotechnical and infrastructural damage due to the 2016 Kumamoto earthquake sequence. *Soil Dyn Earthquake Eng* 104: 390–394.
11. Atkinson GM, Boore DM (1998) Ground-motion relations for eastern North America. *Bull Seismol Soc Am* 85: 17–30.
12. Hwang H, Huo JR (1997) Attenuation relations of ground motion for rock and soil sites in eastern United States. *Soil Dyn Earthquake Eng* 16: 363–372.

13. Toro GR, Abrahamson NA, Schneider JF (1997) Model of strong ground motions from earthquakes in central and eastern North America: Best estimates and uncertainties. *Seismol Res Lett* 68: 41–57.

14. Yoshita M, Okano M, Akiyama H, et al. (1999) A spectral analysis of the 21 May 1997, Jabalpur, India, earthquake (M_w = 5.8) and estimation of ground motion from future earthquakes in the Indian shield region. *Bull Seismol Soc Am* 89: 1620–1630.

15. Iyengar RN, Kanth SR (2004) Attenuation of strong ground motion in peninsular India. *Seismol Res Lett* 75: 530–540.

16. Saragoni GR, Hart FC (1974) Simulation of artificial earthquake accelerograms. *Earthquake Eng Struct Dyn* 2: 249–267.

17. Nau RF, Oliver RM, Pister KS (1982) Simulating and analyzing artificial nonstationary earthquake ground motions. *Bull Seismol Soc Am* 72: 615–636.

18. Kaul MK (1978) Spectrum-consistent time-history generation. *J Eng Mech Div* 104: 781–788.

19. Vanmarcke EH (1979) State-of-the-art for assessing earthquake hazards in the United States. Report 14, representation of earthquake ground motion: Scaled accelerograms and equivalent response spectra. Massachusetts Inst of Tech Cambridge Dept of Civil Engineering.

20. Gasparini DA, Vanmarcke EH (1976) Simulated earthquake motions compatible with prescribed response spectra. Massachusetts Institute of Technology, Department of Civil Engineering, Constructed Facilities Division.

21. Hartzell SH (1978) Earthquake aftershocks as Green's functions. *Geophys Res Lett* 5: 1–4.

22. Irikura K (1983) Semi-empirical estimation of strong ground motions during large earthquakes. *Bull Disaster Prev Res Inst.*

23. Zeng Y, Anderson JG, Yu G (1994) A composite source model for computing realistic synthetic strong ground motions. *Geophys Res Lett* 21: 725–728.

24. Schneider JF, Silva WJ, Stark C (1993) Ground motion model for the 1989 M 6.9 Loma Prieta earthquake including effects of source, path, and site. *Earthquake Spectra* 9: 251–287.

25. Beresnev IA, Atkinson GM (1997) Modeling finite-fault radiation from the ωn spectrum. *Bull Seismol Soc Am* 87: 67–84.

26. Hartzell S, Guatteri M, Mai PM, et al. (2005) Calculation of broadband time histories of ground motion, Part II: Kinematic and dynamic modeling using theoretical Green's functions and comparison with the 1994 Northridge earthquake. *Bull Seismol Soc Am* 95: 614–645.

27. Kristek J, Moczo P (2003) Seismic-wave propagation in viscoelastic media with material discontinuities: A 3D fourth-order staggered-grid finite-difference modeling. *Bull Seismol Soc Am* 93: 2273–2280.

28. Graves RW (1996) Simulating seismic wave propagation in 3D elastic media using staggered-grid finite differences. *Bull Seismol Soc Am* 86: 1091–1106.

29. Pitarka A (1999) 3D elastic finite-difference modeling of seismic motion using staggered grids with nonuniform spacing. *Bull Seismol Soc Am* 89: 54–68.

30. Aoi S, Fujiwara H (1999) 3D finite-difference method using discontinuous grids. *Bull Seismol Soc Am* 89: 918–930.

31. Moczo P, Kristek J, Vavrycuk V, et al. (2002) 3D heterogeneous staggered-grid finite-difference modeling of seismic motion with volume harmonic and arithmetic averaging of elastic moduli and densities. *Bull Seismol Soc Am* 92: 3042–3066.

32. Lee SJ, Chen HW, Huang BS (2008) Simulations of strong ground motion and 3D amplification effect in the Taipei Basin by using a composite grid finite-difference method. *Bull Seismol Soc Am* 98: 1229–1242.

33. Komatitsch D, Liu Q, Tromp J, et al. (2004) Simulations of ground motion in the Los Angeles basin based upon the spectral-element method. *Bull Seismol Soc Am* 94: 187–206.

34. Komatitsch D, Tromp J, Vilotte JP, et al. (2015) The spectral element method for elastic wave equations—application to 2-D and 3-D seismic problems. *Int J Numer Methods Eng* 45: 1139–1164.

35. Priolo E (2001) Earthquake ground motion simulation through the 2-D spectral element method. *J Comput Acoust* 9: 1561–1581.

36. Komatitsch D, Liu Q, Tromp J, et al. (2004) Simulations of ground motion in the Los Angeles basin based upon the spectral-element method. *Bull Seismol Soc Am* 94: 187–206.

37. Lee SJ, Chen HW, Liu Q, et al. (2008) Three-dimensional simulations of seismic-wave propagation in the Taipei basin with realistic topography based upon the spectral-element method. *Bull Seismol Soc Am* 98: 253–264.

38. Stupazzini M, Paolucci R, Igel H (2009) Near-fault earthquake ground-motion simulation in the Grenoble valley by a high-performance spectral element code. *Bull Seismol Soc Am* 99: 286–301.

39. Maechling PJ, Silva F, Callaghan S, et al. (2014) SCEC Broadband Platform: System architecture and software implementation. *Seismol Res Lett* 86: 27–38.

40. Graves R, Pitarka A (2015) Refinements to the Graves and Pitarka (2010) broadband ground-motion simulation method. *Seismol Res Lett* 86: 75–80.

41. Olsen K, Takedatsu R (2015) The SDSU broadband ground-motion generation module BBtoolbox version 1.5. *Seismol Res Lett* 86: 81–88.

42. Crempien JG, Archuleta RJ (2015) UCSB method for simulation of broadband ground motion from kinematic earthquake sources. *Seismol Res Lett* 86: 61–67.

43. Motazedian D, Atkinson GM (2005) Stochastic finite-fault modeling based on a dynamic corner frequency. *Bull Seismol Soc Am* 95: 995–1010.

44. Anderson JG (2015) The composite source model for broadband simulations of strong ground motions. *Seismol Res Lett* 86: 68–74.

45. Boore DM (1983) Stochastic simulation of high-frequency ground motions based on seismological models of the radiated spectra. *Bull Seismol Soc Am* 73: 1865–1894.

46. Boore DM (2003) Simulation of ground motion using the stochastic method. *Pure Appl Geophys* 160: 635–676.

47. Beresnev IA, Atkinson GM (1998) FINSIM—a FORTRAN program for simulating stochastic acceleration time histories from finite faults. *Seismol Res Lett* 69: 27–32.

48. Zonno G, Carvalho A (2006) Modeling the 1980 Irpinia earthquake by stochastic simulation. Comparison of seismic scenarios using finite-fault approaches. InFirst European Conference on Earthquake Engineering and Seismology.

49. Motazedian D, Moinfar A (2006) Hybrid stochastic finite fault modeling of 2003, M6.5, Bam earthquake (Iran). *J Seismol* 10: 91–103.

50. Moratto L, Vuan A, Saraò A (2015) A hybrid approach for broadband simulations of strong ground motion: The case of the 2008 Iwate-Miyagi Nairiku earthquake. *Bull Seismol Soc Am* 105: 2823–2829.

51. Ghofrani H, Atkinson G, Goda K, et al. (2012) Interpreting the 11th March 2011 Tohoku, Japan Earthquake Ground-Motions Using Stochastic Finite-Fault Simulations. Available from:

https://www.researchgate.net/publication/281463795_Interpreting_the_11th_March_2011_Tohoku_Japan_Earthquake_Ground-Motions_Using_Stochastic_Finite-Fault_Simulations.

52. Raghucharan MC, Somala SN (2017) Simulation of strong ground motion for the 25 April 2015 Nepal (Gorkha) M_w 7.8 earthquake using the SCEC broadband platform. *J Seismol* 21: 777–808.

53. Atkinson GM, Assatourians K, Boore DM, et al. (2009) A guide to differences between stochastic point-source and stochastic finite-fault simulations. *Bull Seismol Soc Am* 99: 3192–3201.

54. Aki K (1967) Scaling law of seismic spectrum. *J Geophys Res* 72: 1217–1231.

55. Boore DM (2009) Comparing stochastic point-source and finite-source ground-motion simulations: SMSIM and EXSIM. *Bull Seismol Soc Am* 99: 3202–3216.

56. Atkinson GM, Assatourians K (2015) Implementation and validation of EXSIM (a stochastic finite-fault ground-motion simulation algorithm) on the SCEC broadband platform. *Seismol Res Lett* 86: 48–60.

57. Atkinson GM, Boore DM (2006) Earthquake ground-motion prediction equations for eastern North America. *Bull Seismol Soc Am* 96: 2181–2205.

58. Aoi S, Kunugi T, Fujiwara H (2004) Strong-motion seismograph network operated by NIED: K-Net and KiK-Net. *J Jpn Assoc Earthquake Eng* 4: 65–74.

59. Asano K, Iwata T (2016) Source rupture processes of the foreshock and mainshock in the 2016 Kumamoto earthquake sequence estimated from the kinematic waveform inversion of strong motion data. *Earth Planets Space* 68: 147.

60. Molkenthin C, Scherbaum F, Griewank A, et al. (2014) A study of the sensitivity of response spectral amplitudes on seismological parameters using algorithmic differentiation. *Bull Seismol Soc Am* 104: 2240–2252.

61. J-SHIS (Japan Seismic Hazard Information Station): Subsurface structure of entire Japan. Available from: www.j-shis.bosai.go.jp/map/JSHIS2/download.html?lang=en.

62. Edwards B, Rietbrock A (2009) A comparative study on attenuation and source-scaling relations in the Kantō, Tokai, and Chubu regions of Japan, using data from Hi-Net and KiK-Net. *Bull Seismol Soc Am* 99: 2435–2460.

63. Petukhin A, Kagawa T, Koketsu K, et al. (2011) Construction and waveform testing of the large scale crustal structure model for southwest Japan. InInternational Symposium on Disaster Simulation & Structural Safety in the Next Generation 2011 (DS'11), September 17–18, 2011, Univ. of Hyogo, Kobe, Japan 2011.

64. Huang HC, Teng TL (1999) An evaluation on H/V ratio vs. spectral ratio for site-response estimation using the 1994 Northridge earthquake sequences. *Pure Appl Geophys* 156: 631–649.

65. Yamazaki F, Ansary MA (1997) Horizontal-to-vertical spectrum ratio of earthquake ground motion for site characterization. *Earthquake Eng Struct Dyn* 26: 671–689.

66. Wen KL, Chang TM, Lin CM, et al. (2006) Identification of nonlinear site response using the H/V spectral ratio method. *Terr Atmos Ocean Sci* 17: 533.

67. Bozorgnia Y, Campbell KW (2016) Ground motion model for the vertical-to-horizontal (V/H) ratios of PGA, PGV, and response spectra. *Earthquake Spectra* 32: 951–978.

68. Raghukanth ST, Somala SN (2009) Modeling of strong-motion data in northeastern India: Q, stress drop, and site amplification. *Bull Seismol Soc Am* 99: 705–725.

69. Chen SZ, Atkinson GM (2002) Global comparisons of earthquake source spectra. *Bull Seismol Soc Am* 92: 885–895.

70. Wald DJ, Earle PS, Allen TI, et al. (2008) Development of the US Geological Survey's PAGER system (prompt assessment of global earthquakes for response). *J Autom Chem* 1: 40–42.

71. Boore DM (2010) Orientation-independent, nongeometric-mean measures of seismic intensity from two horizontal components of motion. *Bull Seismol Soc Am* 100: 1830–1835.

72. Abrahamson NA, Silva WJ, Kamai R (2014) Summary of the ASK14 ground motion relation for active crustal regions. *Earthquake Spectra* 30: 1025–1055.

73. Boore DM, Stewart JP, Seyhan E, et al. (2014) NGA-West2 equations for predicting PGA, PGV, and 5% damped PSA for shallow crustal earthquakes. *Earthquake Spectra* 30: 1057–1085.

74. Campbell KW, Bozorgnia Y (2014) NGA-West2 ground motion model for the average horizontal components of PGA, PGV, and 5% damped linear acceleration response spectra. *Earthquake Spectra* 30: 1087–1115.

75. Chiou BS, Youngs RR (2014) Update of the Chiou and Youngs NGA model for the average horizontal component of peak ground motion and response spectra. *Earthquake Spectra* 30: 1117–1153.

76. Zhang L, Chen G, Wu Y, et al. (2016) Stochastic ground-motion simulations for the 2016 Kumamoto, Japan, earthquake. *Earth Planets Space* 68: 184.